Context-Aware Filtering of PolSAR Data Based on Quaternion Wavelet Shrinkage

Yuta Otsuka *Member, IEEE,* Ryo Natsuaki *Senior Member, IEEE,* and Akira Hirose, *Fellow, IEEE*

***Abstract*—Polarimetric synthetic aperture radar (PolSAR) is widely used for land cover classification. One of its major problems is the effect of speckle. Although numerous methods have been developed to suppress speckle noise, it is difficult to classify complex land cover types composed of multiple different scattering mechanisms by pixel-wise classification with existing filtering methods. In this paper, we propose context-aware PolSAR filters based on quaternion wavelet shrinkage to solve this problem. We first represent logarithmic-transformed Stokes vectors (log Stokes vectors) in a quaternion form. Next, we apply the quaternion wavelet transform to the quaternion images of log Stokes vectors. Then, we perform filtering in the quaternion wavelet domain by shrinking small wavelet coefficients. Log Stokes vectors in areas with highly random polarimetric information, i.e., areas where the polarization state varies from pixel to pixel, are strongly filtered, while those in homogeneous areas are weakly filtered or unfiltered. Therefore, after the inverse transform, filtered log Stokes vectors incorporate spatial-context information as the degree of polarization (DoP). This results in accurate classification of complex land cover types without using contextual classifiers or a large number of texture features. Experimental results show that the proposed filters are more suitable than conventional filters for the preprocessing of pixel-wise land cover classification.**

***Index Terms*—Synthetic aperture radar (SAR), Polarimetric synthetic aperture radar (PolSAR), speckle, quaternion, wavelet**

I. Introduction

Polarimetric synthetic aperture radar (PolSAR) is a microwave sensor that uses two polarization modes during transmission and/or reception to get the physical characteristics of ground targets. They are useful for performing land cover classification in various applications such as flood mapping, deforestation detection, and precision agriculture.

PolSAR data, as well as single-polarization synthetic-aperture-radar (SAR) data, are affected by speckle. Speckle is inherent in SAR observation due to the interference of scattered waves from a large number of scatterers within a resolution cell. It appears as the fluctuations of amplitude and phase values [1], [2], which reduce the accuracy of land cover classification.

In order to suppress the effect of speckle, numerous filtering methods have been proposed. The boxcar filter is the simplest method among them. It performs the averaging of a target pixel with neighboring pixels inside a window. Since the window size is fixed, there is a tradeoff between speckle reduction and edge preservation. To overcome this limitation, filtering methods based on adaptive windows have been investigated. Lee et al. [3] proposed the extended sigma filter, which performs filtering by using only pixels within a certain range of intensity values. Vasile et al. [4] developed the adaptive neighborhood technique, which determines a window shape based on intensity values, for the estimation of PolSAR parameters. Nonlocal filtering methods [5], [6] have also been utilized for PolSAR. They achieved high speckle-reduction abilities without losing edge features by using only homogenous pixels in a large search window for filtering. Recently, filtering methods based on convolutional neural networks (CNNs) have been developed. Tucker et al. [7] used real-valued CNNs to filter PolSAR data, while Mullissa et al. [8] adopted complex-valued CNNs to take into account the relationship between the real and imaginary components. Lin et al. [9] utilized CNNs to estimate the weights for nonlocal filtering.

These advanced methods based on adaptive windows, nonlocal filtering, or CNNs aim to filter a target pixel through weighted or non-weighted averaging with homogeneous pixels, that is, pixels with the same scattering mechanism. Therefore, it is difficult to directly conduct pixel-wise land cover classification by using the filtered data from these methods since some land cover types contain multiple different scattering mechanisms. For instance, sparsely vegetated areas possibly contain three scattering mechanisms, namely, surface scattering from the ground surface, double-bounce scattering due to the dihedral of the ground surface and vegetation, and volume scattering from vegetation.

To accurately classify complex land cover types, spatial-context information needs to be utilized. The methods to incorporate spatial-context information into PolSAR land cover classification can be categorized into two groups. The first group extracts texture features from PolSAR data and uses them as inputs to pixel-wise classifiers. Texture features, including wavelet coefficients [10], [11] and gray level cooccurrence matrix (GLCM) [12], have been found useful for accurate classification. However, this approach requires a large number of texture features to realize accurate classification.

A part of this work was presented in International Geoscience and Remote Sensing Symposium (IGARSS) 2025, Brisbane, Australia. This work was supported in part by the Japan Society for the Promotion of Science (JSPS) KAKENHI Grant Number 23H00487; the Remote Sensing Technology Center of Japan (RESTEC); and in part by the Cooperative Research Project Program of the Research Institute of Electrical Communication (RIEC), Tohoku University. The RADARSAT-2 and F-SAR original data are publicly available at https://ietr-lab.univ-rennes1.fr/polsarpro-bio/san-francisco/ and https://doi.org/10.35097/1700, respectively.

Y. Otsuka was with the Department of Electrical Engineering and Information Systems, The University of Tokyo, Tokyo 113-8656, Japan, and is presently with Microwaves and Radar Institute, German Aerospace Center (DLR), 82234 Weßling, Germany (e-mail: yuta.otsuka@dlr.de).

R. Natsuaki and A. Hirose are with the Department of Electrical Engineering and Information Systems, The University of Tokyo, Tokyo 113-8656, Japan (e-mail: natsuaki@ee.t.u-tokyo.ac.jp; ahirose@ee.t.u-tokyo.ac.jp).

Hence, classification methods based on texture features demand a large amount of labeled PolSAR data, which is mostly unavailable. The second group uses contextual classifiers instead of pixel-wise classifiers. Contextual classifiers perform land cover classification based on features of not only a target pixel, but also neighboring pixels [11], [13]. Among them, many classifiers based on CNNs have been reported in recent years. Zhou et al. [14] applied CNNs to incorporate hierarchical spatial information into PolSAR land cover classification. Jamali et al. [15] combined CNNs with wavelet transform to further improve classification accuracy. However, these contextual classifiers require more labeled PolSAR data than pixel-wise classifiers since the number of input features increases as the number of pixels used for classification becomes larger.

To perform accurate land cover classification even with limited labeled data, we propose context-aware PolSAR filters based on quaternion wavelet shrinkage. They first represent logarithmic-transformed Stokes vectors (log Stokes vectors) in the quaternion form [16], [17]. Next, the quaternion wavelet transform [18], [19] is applied to the quaternion images of log Stokes vectors. Then, we perform filtering in the quaternion wavelet domain by shrinking small wavelet coefficients [20]. In contrast to conventional filtering methods using size-limited windows, the proposed methods filter all the pixels of an entire image simultaneously. Log Stokes vectors in areas with highly random polarimetric information, i.e., areas where the polarization state varies from pixel to pixel, are strongly filtered, while those in homogenous areas are weakly filtered or unfiltered. Therefore, after the inverse transform, filtered log Stokes vectors incorporate spatial-context information as the degree of polarization. This spatial-context information enables the pixel-wise classification of complex land cover types without using a large number of texture features or contextual classifiers, which are required by conventional filtering methods based on size-limited windows. Hence, high classification accuracy can be achieved even when the amount of labeled PolSAR data is limited. We evaluate the proposed methods by the experiments of land cover classification and the analysis of filtering results.

This paper is organized as follows. In Section II, we explain the quaternion wavelet transform. Section III introduces context-aware PolSAR filters based on quaternion wavelet shrinkage. Section IV shows the evaluation of the proposed methods. Section V concludes this paper.

II. Quaternion wavelet transform

A. Introduction to quaternion

Quaternion is one of the hypercomplex numbers. It consists of four components as

$$\begin{aligned}\mathbf{q} &= q_0 + q_1\mathbf{i} + q_2\mathbf{j} + q_3\mathbf{k} \\ &= (q_0, q_1, q_2, q_3)\end{aligned} \tag{1}$$

where $\mathbf{i}$, $\mathbf{j}$ and $\mathbf{k}$ are imaginary units, and q_0, q_1, q_2, and q_3 are real numbers.

We introduce the operations of quaternions as follows. The summation and subtraction are defined as

$$\mathbf{p} \pm \mathbf{q} = (p_0 \pm q_0, p_1 \pm q_1, p_2 \pm q_2, p_3 \pm q_3) \tag{2}$$

The Hamilton product is defined as

$$\begin{aligned}\mathbf{pq} = (&p_0q_0 - p_1q_1 - p_2q_2 - p_3q_3, \\ &p_0q_1 + p_1q_0 + p_2q_3 - p_3q_2, \\ &p_0q_2 + p_2q_0 + p_3q_1 - p_1q_3, \\ &p_0q_3 + p_3q_0 + p_1q_2 - p_2q_1)\end{aligned} \tag{3}$$

It is important to note that the Hamilton product is not commutative, that is, $\mathbf{pq} \neq \mathbf{qp}$. The conjugation is defined as

$$\overline{\mathbf{q}} = (q_0, -q_1, -q_2, -q_3) \tag{4}$$

The norm is defined as

$$\|\mathbf{q}\| = \sqrt{q_0^2 + q_1^2 + q_2^2 + q_3^2} \tag{5}$$

B. Quaternion wavelet transform

Wavelet transform is an effective method to analyze a signal whose spectral information changes with time or position. Its extension to the quaternion domain is known as the quaternion wavelet transform (QWT) [18], [21]. A quaternion-valued signal $\mathbf{f}(t)$ is decomposed by the QWT with a scaling function $\boldsymbol{\phi}(t)$ and a wavelet function $\boldsymbol{\psi}(t)$, which extract smooth and detailed components, respectively, as

$$\begin{aligned}\mathbf{f}(t) &= \sum_k \mathbf{s}_k^{(J)} \boldsymbol{\phi}_{J,k}(t) + \sum_{j=1}^{J}\sum_k \mathbf{w}_k^{(j)} \boldsymbol{\psi}_{j,k}(t) \\ \boldsymbol{\phi}_{j,k}(t) &= 2^{-\frac{j}{2}}\boldsymbol{\phi}(2^{-j}t - k) \\ \boldsymbol{\psi}_{j,k}(t) &= 2^{-\frac{j}{2}}\boldsymbol{\psi}(2^{-j}t - k)\end{aligned} \tag{6}$$

where j and k are scale and translation parameters, respectively, and $\mathbf{s}_k^{(J)}$ and $\mathbf{w}_k^{(j)}$ are scaling and wavelet coefficients, respectively.

The decomposition can be performed efficiently by using the quaternion extension of the Mallat algorithm [22]. This algorithm iteratively computes the scaling and wavelet coefficients of each decomposition level using the coefficients of the previous decomposition level as

$$\begin{aligned}\mathbf{s}_k^{(j)} &= \sum_u \mathbf{s}_u^{(j-1)} \overline{\mathbf{a}_{u-2k}} \\ \mathbf{w}_k^{(j)} &= \sum_u \mathbf{s}_u^{(j-1)} \overline{\mathbf{b}_{u-2k}}\end{aligned} \tag{7}$$

where $\mathbf{a}_{u-2k}$ and $\mathbf{b}_{u-2k}$ are the scaling and wavelet sequences, respectively, which give the two-scale relations as

$$\begin{aligned}\boldsymbol{\phi}_{j,k}(t) &= \sum_u \mathbf{a}_{u-2k}\boldsymbol{\phi}_{j-1,u}(t) \\ \boldsymbol{\psi}_{j,k}(t) &= \sum_u \mathbf{b}_{u-2k}\boldsymbol{\phi}_{j-1,u}(t)\end{aligned} \tag{8}$$

If the scaling function cannot be expressed in a closed form, the scaling coefficients of the finest scale can be approximated as $\mathbf{s}_k^{(0)} \simeq \mathbf{f}(k)$ since the scaling function can be approximated to the delta function at a fine enough scale.

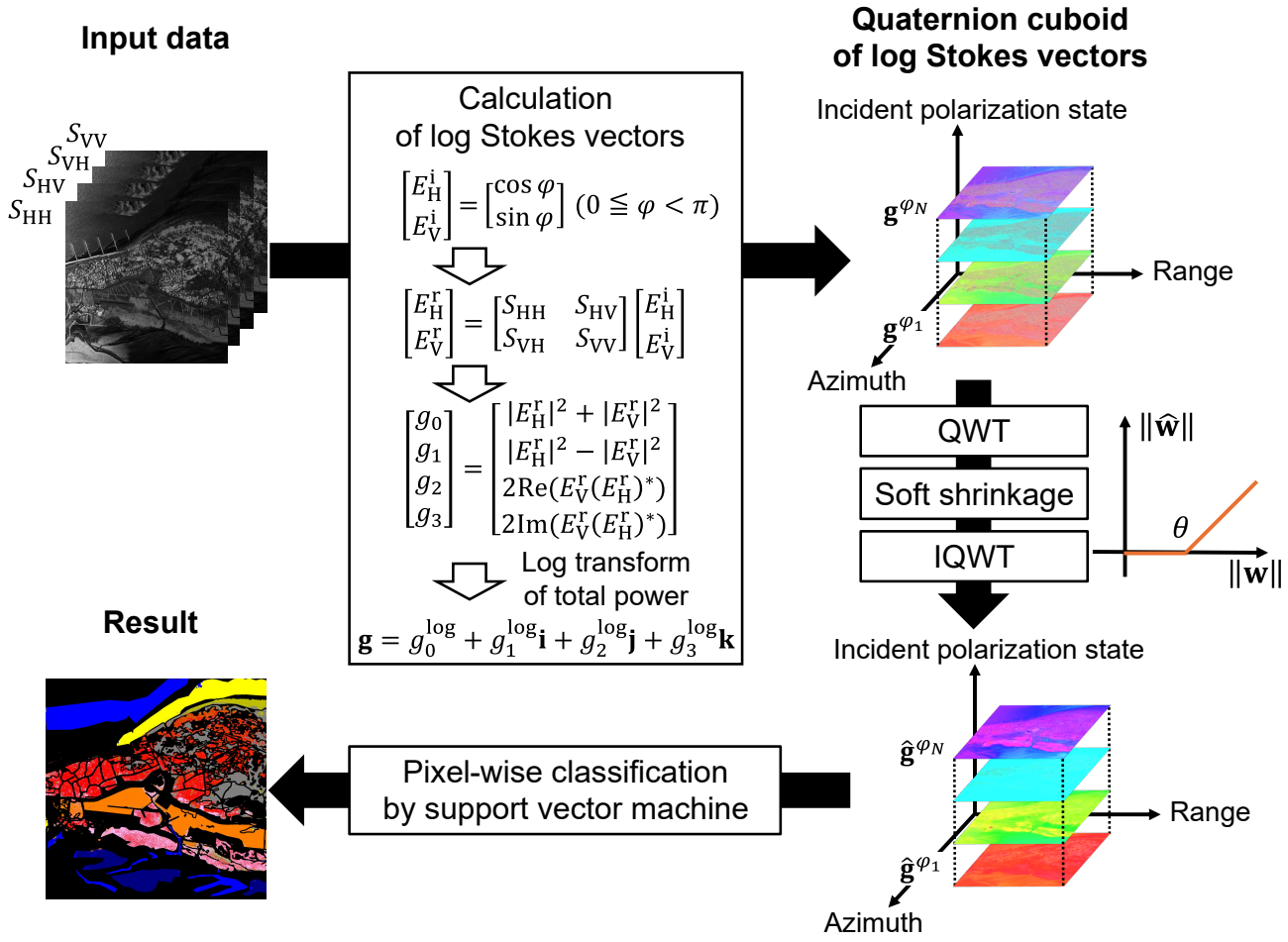

Fig. 1: PolSAR land cover classification based on quaternion wavelet shrinkage, where the polarization states of log Stokes vectors are represented by the hue-saturation-lightness (HSL) color space.

The inverse quaternion wavelet transform (IQWT) is performed as

$$\mathbf{s}_k^{(j-1)} = \sum_u (\mathbf{s}_u^{(j)} \mathbf{a}_{k-2u} + \mathbf{w}_u^{(j)} \mathbf{b}_{k-2u}) \tag{9}$$

In both QWT and IQWT, the order of the Hamilton-product operands cannot be changed due to the noncommutativity of the operation.

III. Context-aware PolSAR filtering based on quaternion wavelet shrinkage

A. Stokes-vector representation of PolSAR data

Fig. 1 shows the processing flow of PolSAR land cover classification based on the quaternion wavelet shrinkage (QWS). PolSAR first measures a scattering matrix for each resolution cell, which is defined as

$$\begin{bmatrix} E_H^r \\ E_V^r \end{bmatrix} = \begin{bmatrix} S_{HH} & S_{HV} \\ S_{VH} & S_{VV} \end{bmatrix} \begin{bmatrix} E_H^i \\ E_V^i \end{bmatrix} \tag{10}$$

where H and V represent horizontal and vertical polarization modes, respectively, and $[E_H^i \; E_V^i]^T$ and $[E_H^r \; E_V^r]^T$ are incident and recieved waves, respectively.

The single-look Stokes vector can be computed as

$$\begin{bmatrix} g_0 \\ g_1 \\ g_2 \\ g_3 \end{bmatrix} = \begin{bmatrix} |E_H^r|^2 + |E_V^r|^2 \\ |E_H^r|^2 - |E_V^r|^2 \\ 2\mathrm{Re}(E_V^r (E_H^r)^*) \\ 2\mathrm{Im}(E_V^r (E_H^r)^*) \end{bmatrix} \tag{11}$$

where $|\cdot|$ means the absolute value. Four components g_0, g_1, g_2 and g_3 represent the total power, the power difference between horizontal and vertical polarization elements, that of 45° and 135° linear polarization elements, and that of left-handed and right-handed circular polarization elements. The last three components can be normalized by the total power as

$$\begin{bmatrix} x \\ y \\ z \end{bmatrix} = \begin{bmatrix} \frac{g_1}{g_0} & \frac{g_2}{g_0} & \frac{g_3}{g_0} \end{bmatrix}^T \tag{12}$$

This represents a point on a unit sphere known as the Poincare sphere. Therefore, we call this vector a Poincare vector in this paper. The degree of polarization (DoP) of a single-look Poincare vector is unity, i.e., $\mathrm{DoP} = \sqrt{x^2 + y^2 + z^2} = 1$.

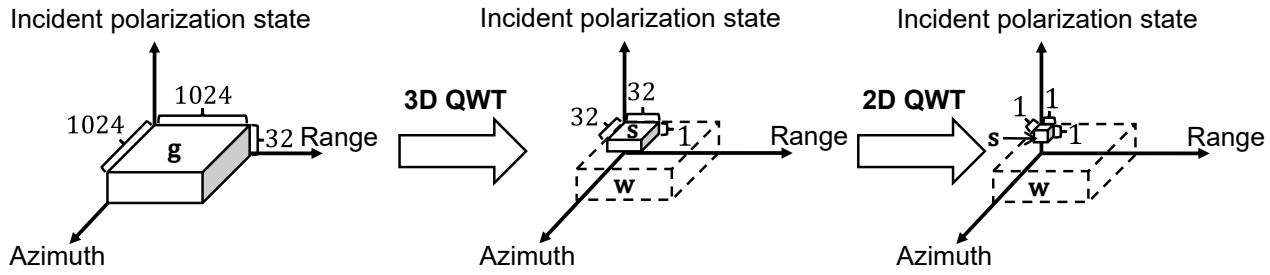

Fig. 2: Decomposition procedure of 3D QWS, where the size of input data is 1024×1024×32.

We combine the single-look Poincare vector with logarithmically transformed total power as

$$\begin{bmatrix} g_0^{\log} \\ g_1^{\log} \\ g_2^{\log} \\ g_3^{\log} \end{bmatrix} = \frac{g_0^{\log}}{g_0} \begin{bmatrix} g_0 \\ g_1 \\ g_2 \\ g_3 \end{bmatrix} \tag{13}$$
$$g_0^{\log} = \log_e g_0 - \log_e g_0^{\min}$$

where $g_0^{\min}$ is the minimum value of the total power among all pixels. We call this vector a log Stokes vector in this paper. The logarithmic transform changes the multiplicative nature of the speckle effect on the total power to the additive nature, which is suitable for wavelet shrinkage. The log Stokes vector of each pixel can be stored in a quaternion as

$$\mathbf{g} = g_0^{\log} + g_1^{\log}\mathbf{i} + g_2^{\log}\mathbf{j} + g_3^{\log}\mathbf{k} \tag{14}$$

B. Filtering by 2D quaternion wavelet shrinkage

A quaternion image of log Stokes vectors can be filtered by two-dimensional quaternion wavelet shrinkage (2D QWS). It first applies a two-dimensional QWT (2D QWT) to the quaternion image as

$$\begin{aligned} \mathbf{g}(p,q) = &\sum_k \sum_l \mathbf{s}_{k,l}^{(J)} \mathbf{\Phi}_{J,k,l}(p,q) \\ &+ \sum_{i=H,V,D} \sum_{j=1}^{J} \sum_k \sum_l \mathbf{w}_{k,l}^{(j,i)} \mathbf{\psi}_{j,k,l}^{i}(p,q) \end{aligned} \tag{15}$$

where (p,q) is the pixel position, k and l are translation parameters, and H, V and D represent horizontal, vertical and diagonal directions, respectively. The scaling and wavelet coefficients are computed as

$$\begin{aligned} \mathbf{s}_{k,l}^{(j)} &= \sum_v \sum_u \mathbf{s}_{u,v}^{(j-1)} \overline{\mathbf{a}_{u-2k}}\, \overline{\mathbf{a}_{v-2l}} \\ \mathbf{w}_{k,l}^{(j,H)} &= \sum_v \sum_u \mathbf{s}_{u,v}^{(j-1)} \overline{\mathbf{a}_{u-2k}}\, \overline{\mathbf{b}_{v-2l}} \\ \mathbf{w}_{k,l}^{(j,V)} &= \sum_v \sum_u \mathbf{s}_{u,v}^{(j-1)} \overline{\mathbf{b}_{u-2k}}\, \overline{\mathbf{a}_{v-2l}} \\ \mathbf{w}_{k,l}^{(j,D)} &= \sum_v \sum_u \mathbf{s}_{u,v}^{(j-1)} \overline{\mathbf{b}_{u-2k}}\, \overline{\mathbf{b}_{v-2l}} \\ \mathbf{s}_{k,l}^{(0)} &= \mathbf{g}(k,l) \end{aligned} \tag{16}$$

Speckle is suppressed by soft shrinkage [23] in the quaternion wavelet domain as

$$\hat{\mathbf{w}}_{k,l}^{(j,i)} = \begin{cases} (1 - \frac{\theta}{\|\mathbf{w}_{k,l}^{(j,i)}\|})\mathbf{w}_{k,l}^{(j,i)} & \|\mathbf{w}_{k,l}^{(j,i)}\| > \theta \\ 0 & \|\mathbf{w}_{k,l}^{(j,i)}\| \leqq \theta \end{cases} \tag{17}$$

where θ is the threshold of soft shrinkage.

Finally, two-dimensional IQWT produces the quaternion image of filtered log Stokes vectors $\hat{\mathbf{g}}(p,q)$ as

$$\begin{aligned} \hat{\mathbf{s}}_{k,l}^{(j-1)} = &\sum_u \sum_v (\hat{\mathbf{s}}_{u,v}^{(j)} \mathbf{a}_{l-2v}\mathbf{a}_{k-2u} + \hat{\mathbf{w}}_{u,v}^{(j,H)} \mathbf{b}_{l-2v}\mathbf{a}_{k-2u} \\ &+ \hat{\mathbf{w}}_{u,v}^{(j,V)} \mathbf{a}_{l-2v}\mathbf{b}_{k-2u} + \hat{\mathbf{w}}_{u,v}^{(j,D)} \mathbf{b}_{l-2v}\mathbf{b}_{k-2u}) \\ \hat{\mathbf{g}}(p,q) = &\hat{\mathbf{s}}_{p,q}^{(0)} \end{aligned} \tag{18}$$

where the scaling coefficients of the coarsest scale are unchanged, $\hat{\mathbf{s}}_{k,l}^{(J)} = \mathbf{s}_{k,l}^{(J)}$.

The QWT processes a log Stokes vector as a single entity instead of processing each component of the vector independently. Log Stokes vectors in areas with highly random polarimetric information, i.e., areas where the polarization state varies from pixel to pixel, are represented by small wavelet coefficients, while those in homogeneous areas are represented by large wavelet coefficients. The former are strongly filtered by the shrinkage, while the latter are weakly filtered or unfiltered. Before the shrinkage, all the DoP values of single-look log Stokes vectors are unity. After the shrinkage, we can calculate a value equivalent to the DoP. Then, the strong filtering in the former results in low DoP values, while the weak filtering or unfiltering in the latter results in high DoP values. This means that filtered log Stokes vectors incorporate spatial-context information as DoP values, which make it possible to accurately classify complex land cover types composed of multiple different scattering mechanisms.

C. Filtering by 3D quaternion wavelet shrinkage

If we consider different incident polarization states to calculate Stokes vectors, multiple quaternion images of log Stokes vectors can be obtained. The 3D quaternion wavelet shrinkage (3D QWS) is useful for filtering these images holistically. Here, we extend the 2D QWT to the 3D quaternion wavelet transform (3D QWT). If the input data is cubic, the 3D QWT can be applied until the coarsest scale, where a single voxel represents the scaling coefficient. However, if the number of incident polarization states is smaller than the azimuth and

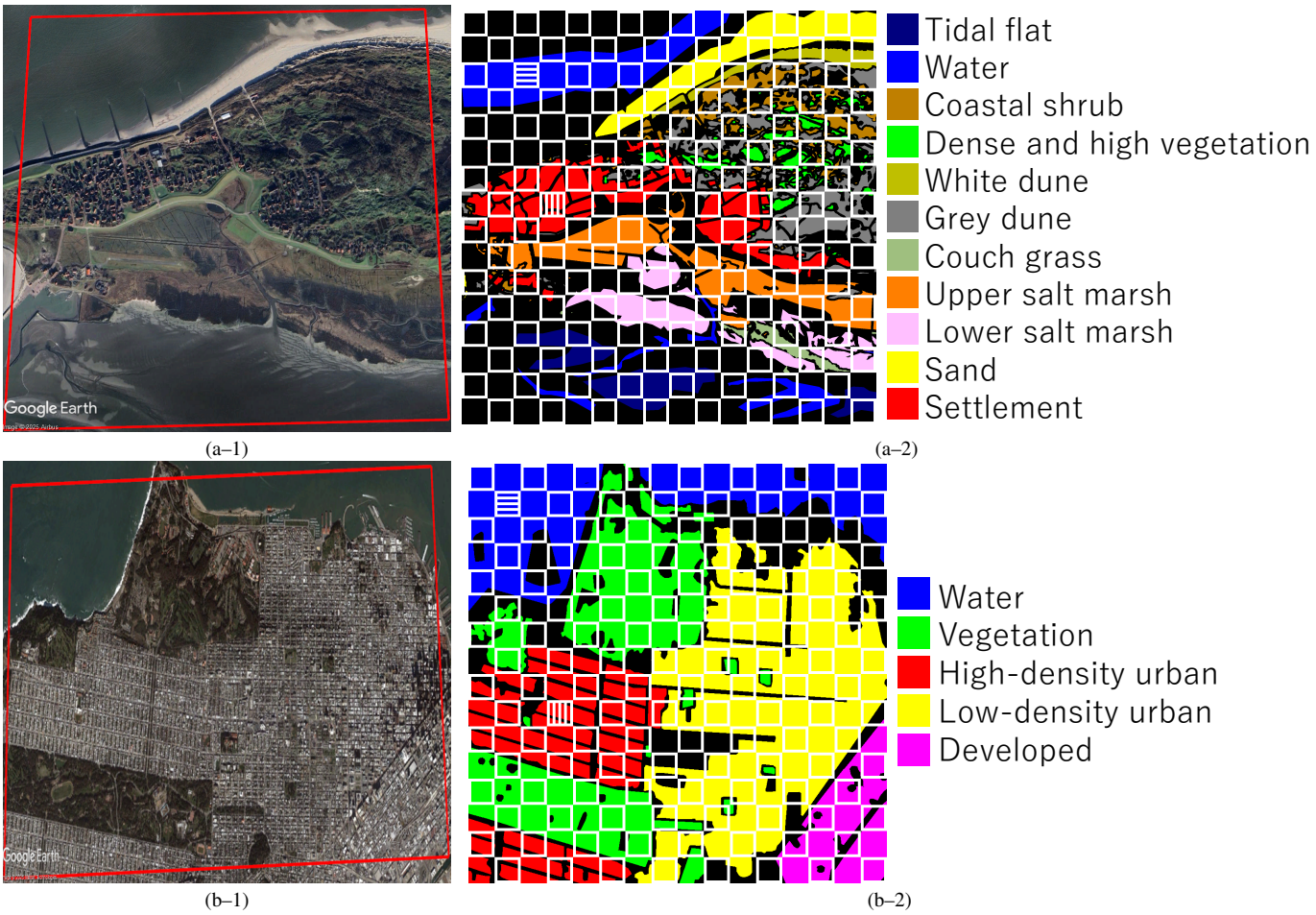

Fig. 3: ($\star$-1) Optical images of the observed scenes (red rectangles) and ($\star$-2) their ground-truth maps with white rectangles enclosing training pixels ((a-$\star$) Baltrum and (b-$\star$) San Francisco datasets).

range pixel numbers, the 3D QWT can be applied only until a certain scale J^{3D}, where the scaling coefficients become two-dimensional, as

$$\begin{aligned}\mathbf{g}(p,q,r) = &\sum_{k}\sum_{l}\mathbf{s}^{(J^{\mathrm{3D}})}_{k,l,1}\boldsymbol{\Phi}_{J^{\mathrm{3D}},k,l,1}(p,q,r)\\ &+\sum_{i=1}^{7}\sum_{j=1}^{J^{\mathrm{3D}}}\sum_{k}\sum_{l}\sum_{m}\mathbf{w}^{(j,i)}_{k,l,m}\boldsymbol{\Psi}^{i}_{j,k,l,m}(p,q,r)\end{aligned} \tag{19}$$

where (p,q,r) is the voxel position, and k, l, and m are translation parameters. Then, the 2D QWT is applied until the coarsest scale J^{2D} as

$$\begin{aligned}\mathbf{s}^{(J^{\mathrm{3D}})}_{k,l,1} = &\sum_{u}\sum_{v}\mathbf{s}^{(J^{\mathrm{2D}})}_{u,v}\boldsymbol{\Phi}_{J^{\mathrm{2D}},u,v}(k,l)\\ &+\sum_{i=H,V,D}\sum_{j=1}^{J^{\mathrm{2D}}}\sum_{u}\sum_{v}\mathbf{w}^{(j,i)}_{u,v}\boldsymbol{\Psi}^{i}_{j,u,v}(k,l)\end{aligned} \tag{20}$$

This procedure is illustrated in Fig. 2. The inverse transform is conducted by the 2D and 3D IQWT in this order.

TABLE I: Details of the two datasets.

Parameters	Baltrum dataset	San Francisco dataset
Sensor	F-SAR	RADARSAT-2
Frequency band	S	C
Acquisition time	April, 2022	April, 2008
Location	Baltrum, Germany	San Francisco, USA
Spatial resolution	1 [m]	8 [m]
Size	2048×2048 [pixels]	1024×1024 [pixels]
Central coordinates	(53°43'38"N, 7°22'45"E)	(37°47'15"N, 122°27'15"W)

IV. Experiments

A. Experimental setup

1) Implementation details of the 2D and 3D QWS: In order to evaluate the effectiveness of the 2D and 3D QWS, we conduct pixel-wise land cover classification by using filtered log Stokes vectors as shown in Fig. 1. In the case of the 2D QWS, we use four incident polarization states to produce four quaternion images, namely, horizontal wave $[1\ 0]^{\mathrm{T}}$, vertical wave $[0\ 1]^{\mathrm{T}}$, 45° linear polarized wave $\left[\frac{1}{\sqrt{2}}\ \frac{1}{\sqrt{2}}\right]^{\mathrm{T}}$ and 135° linear polarized wave $\left[\frac{-1}{\sqrt{2}}\ \frac{1}{\sqrt{2}}\right]^{\mathrm{T}}$. We apply the 2D QWS to each entire quaternion image. The number of input features to a pixel-wise classifier is 16, since each log Stokes vector has

4 real-valued coefficients. In the case of the 3D QWS, we use 32 linear incident polarization states, which are calculated as

$$\begin{bmatrix} E_{\mathrm{H}}^{\mathrm{i}} \\ E_{\mathrm{V}}^{\mathrm{i}} \end{bmatrix} = \begin{bmatrix} \cos\frac{(i-1)\pi}{32} \\ \sin\frac{(i-1)\pi}{32} \end{bmatrix} (i = \{1, 2, \cdots, 32\}) \tag{21}$$

We apply the 3D QWS to the entire quaternion cuboid of log Stokes vectors. After the filtering by the 3D QWS, we use only the log Stokes vectors of the same four incident polarization states as those of the 2D QWS for the input features to the classifier.

The other implementation details of the QWS are as follows. We use the quaternion wavelet proposed by Ginzberg et al. [19] for the QWS. We set the percentages of thresholded wavelet coefficients among all wavelet coefficients as 90% and 99% for the 2D and 3D QWS, respectively, considering that the 3D QWT enables a more sparse representation than the 2D QWT. We implement the QWS using the Quaternion Toolbox for Matlab [24].

2) Conventional methods used for comparison: For the comparison with conventional methods, we use the refined Lee filter [25], the extended sigma filter [3], and the pretest filter [5]. The three filters are first applied to Stokes vectors. Then, filtered Stokes vectors are converted to log Stokes vectors. The window sizes of the refined Lee filter, the extended sigma filter, and the pretest filter are set to 13x13 pixels, 15x15 pixels, and 25x25 pixels, respectively. The patch size of the pretest filter is set to 3×3 pixels. We set the window sizes based on how effectively they conduct the homogeneous-pixel selection. The refined Lee filter uses eight predefined edge-aligned windows, while the extended sigma filter and the pretest filter select pixels inside the search window based on a certain metric. Therefore, the refined Lee filter is less adaptive than the others. The homogeneous-pixel selection of the pretest filter is more effective than that of the extended sigma filter because the former uses the patch similarity, while the latter uses only the intensity of the pixel itself. Thus, the window size of the pretest filter is set to the largest, while that of the refined Lee filter is set to the smallest.

3) Datasets: We use two PolSAR datasets for land cover classification. The first dataset is S-band data obtained over Baltrum, Germany, by Flugzeug-SAR (F-SAR), which is an airborne SAR system of the German Aerospace Center (DLR). The second dataset is C-band data obtained over San Francisco, the USA, by RADARSAT-2, which is a spaceborne SAR system of the Canadian Space Agency (CSA). We call the first and second datasets the Baltrum and San Francisco datasets, respectively. The sizes of the Baltrum and San Francisco datasets are 2048×2048 pixels and 1024×1024 pixels, respectively. The filtering intensity parameter K of the pretest filter is set to 800 and 1800 for the Baltrum and San Francisco datasets, respectively, in order to use about half of the pixels in a search window as homogeneous pixels. Further details of the datasets are shown in Table I.

Fig. 3(⋆-1) shows the optical images for the observed scenes of the Baltrum and San Francisco datasets, acquired in February 2025 and February 2008, respectively. Ground truth data for the first dataset are provided by Hochstuhl et al. [26], while Liu et al. [27] provided ground truth data for the second dataset. As shown in Fig. 3(⋆-2), each dataset is first split into 16×16 areas. Then, half of the areas are used for training, while the rest of the areas are used for testing. We use a linear support vector machine as a classifier.

B. Classification results

Fig. 4 and Table II show the classification maps and the quantitative evaluation results of the Baltrum dataset. It is evident from Table II that the 2D and 3D QWS show higher overall accuracy than the conventional methods. Specifically, the proposed methods have higher recall values for the classes with complex land cover types, such as the White dune class. The White dune class consists of different scattering mechanisms. It has multiple meter-high dunes covered by more or less open low-growing vegetation [26]. The use of the spatial-context information improves the classification of this complex land cover type.

Fig. 5 and Table III show the classification maps and the quantitative evaluation results of the San Francisco dataset. The proposed methods present higher overall accuracy than the conventional methods. However, the 2D QWS shows a lower recall value than the recall values of the refined Lee filter, the pretest filter, and the 3D QWS for the Vegetation class. This is because the high speckle-suppression ability of the 2D QWS leads to the loss of local features, including small Vegetation areas. The 3D QWS has more pixels correctly classified in these small Vegetation areas than the 2D QWS.

C. Evaluation of filtering performance

1) Filtering-performance metrics: We also evaluate the filtering performance of the 2D and 3D QWS by using four filtering-performance metrics. Two of them are widely used metrics, namely, the equivalent number of looks (ENL) [28] and the edge preservation index (EPI) [29]. The ENL is used to evaluate the speckle-reduction ability, which is calculated in a homogeneous area as

$$\mathrm{ENL} = \frac{1}{\mathrm{var}(\hat{g}_0^{\log})} \tag{22}$$

where $\hat{g}_0^{\log}$ is the total power of the filtered log Stokes-vector, and var$(\cdot)$ is the variance in the area. Note that the numerator of the ENL is set to 1 instead of the square of the mean because there are large differences in the mean values of different filtering methods due to the difference of $g_0^{\min}$ in (13).

The EPI is used to evaluate the edge-preservation ability. The EPI for the horizontal and vertical directions, which we name EPI-H and EPI-V, respectively, are calculated in an area with edge features as

$$\begin{aligned} \text{EPI-H} &= \frac{\sum_p \sum_q \left| \sum_{i=-N}^{N} \hat{g}_0^{\log}(p, q+i) - \sum_{i=-N}^{N} \hat{g}_0^{\log}(p+1, q+i) \right|}{\sum_p \sum_q \left| \sum_{i=-N}^{N} g_0^{\log}(p, q+i) - \sum_{i=-N}^{N} g_0^{\log}(p+1, q+i) \right|} \\ \text{EPI-V} &= \frac{\sum_p \sum_q \left| \sum_{i=-N}^{N} \hat{g}_0^{\log}(p+i, q) - \sum_{i=-N}^{N} \hat{g}_0^{\log}(p+i, q+1) \right|}{\sum_p \sum_q \left| \sum_{i=-N}^{N} g_0^{\log}(p+i, q) - \sum_{i=-N}^{N} g_0^{\log}(p+i, q+1) \right|} \end{aligned} \tag{23}$$

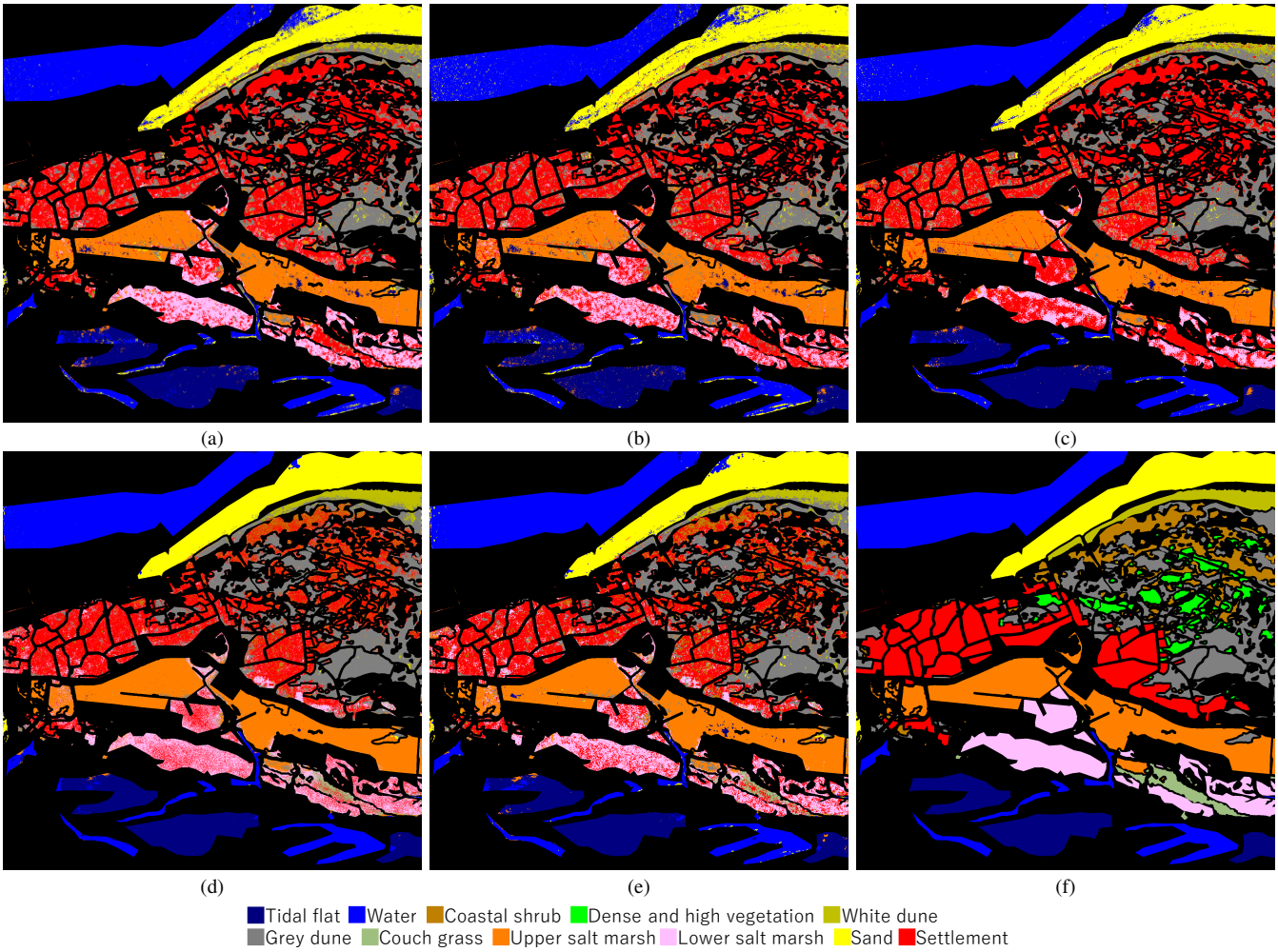

Fig. 4: Classification maps of Baltrum dataset ((a) Refined Lee filter, (b) Extended sigma filter, (c) Pretest filter, (d) 2D QWS, (e) 3D QWS, and (f) Ground truth).

TABLE II: Quantitative evaluation of classification results of Baltrum dataset (TF: Tidal flat, W: Water, CS: Costal shrub, DV: Dense and high vegetation, WD: White dune, GD: Grey dune, CG: Couch grass, US: Upper salt marsh, LS: Lower salt marsh, S: Sand, SE: Settlement, OA: Overall accuracy, and KC: Kappa coefficient).

Method	Recall [%]											OA [%]	KC
	TF	W	CS	DV	WD	GD	CG	US	LS	S	SE		
Refined Lee	91.67	94.64	0.16	0.01	25.65	79.08	3.53	83.38	69.64	84.03	76.24	73.62	0.70
Extended sigma	88.88	92.39	0.03	0.12	20.03	75.19	1.50	78.88	55.93	84.22	75.10	70.24	0.66
Pretest	94.86	96.85	0.05	0.01	26.81	79.07	0.35	85.76	40.24	88.91	73.47	71.87	0.67
2D QWS	97.01	98.50	30.62	0.56	59.73	82.67	26.43	89.70	61.14	97.61	73.52	79.11	0.76
3D QWS	93.94	97.83	31.01	1.13	48.17	82.86	27.35	87.32	63.48	94.73	71.99	77.84	0.75

where p and q are the pixel positions in the area, and the summation $\sum_{i=-N}^{N}(\cdot)$ is performed to mitigate the speckle effect on the EPI estimation. We set N to 4 in this paper.

In addition to the ENL and the EPI, we introduce two metrics, namely, the target-to-clutter difference (TCD) and the polarimetric ENL (PolENL). We define the TCD by adjusting the target-to-clutter ratio (TCR) [28], which is used to evaluate the point-target preservation, to log Stokes vectors. It is calculated as

$$\begin{aligned}\mathrm{TCD} = &\big|(\max(\hat{g}_0^{\log}) - \mathrm{mean}(\hat{g}_0^{\log})) \\ &- (\max(g_0^{\log}) - \mathrm{mean}(g_0^{\log}))\big|\end{aligned} \tag{24}$$

where $\max(\cdot)$ and $\mathrm{mean}(\cdot)$ are the max and mean values in a patch containing a point target, respectively. The TCD is averaged over multiple patches with point targets. The patch size is set to 15×15 pixels. The PolENL is used to measure the speckle reduction in polarimetric information, which is also calculated in a homogeneous region as

$$\mathrm{PolENL} = \frac{1}{\sum_{i=1}^{3} \mathrm{var}(\frac{\hat{g}_i^{\log}}{\hat{g}_0^{\log}})}. \tag{25}$$

2) Evaluation results: Table IV and V show the evaluation results of filtering performance in the Baltrum and San Francisco datasets, respectively. The ENL and PolENL are

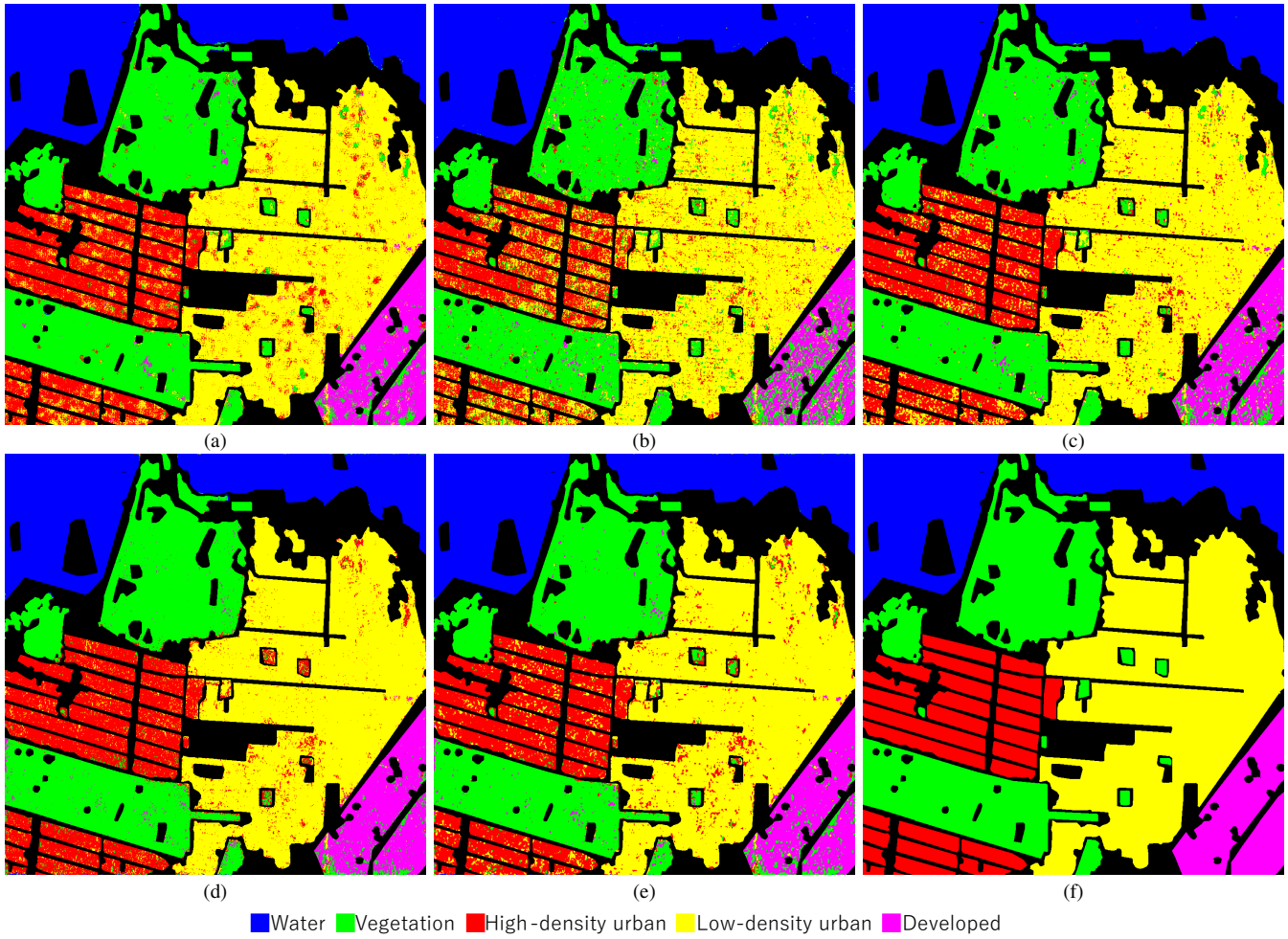

Fig. 5: Classification maps of San Francisco dataset ((a) Refined Lee filter, (b) Extended sigma filter, (c) Pretest filter, (d) 2D QWS, (e) 3D QWS, and (f) Ground truth).

TABLE III: Quantitative evaluation of classification results of San Francisco dataset (W: Water, V: Vegetation, HU: High-density urban, LU: Low-density urban, D: Developed, OA: Overall accuracy, and KC: Kappa coefficient).

Method	Recall [%]					OA [%]	KC
	W	V	HU	LU	D		
Refined Lee	99.80	97.10	81.86	92.44	85.70	92.89	0.91
Extended sigma	99.84	93.86	65.01	89.72	66.80	87.27	0.83
Pretest	99.91	96.94	81.74	93.63	82.39	93.02	0.91
2D QWS	99.85	95.57	91.09	96.17	88.93	95.43	0.94
3D QWS	99.88	96.55	89.28	94.95	86.14	94.78	0.93

TABLE IV: Quantitative evaluation of filtering performance in Baltrum dataset.

Method	ENL	PolENL	EPI-H	EPI-V	TCD
Refined Lee	11.5	474.9	0.54	0.41	1.67
Extended sigma	5.5	260.3	0.63	0.51	0.61
Pretest	16.8	919.2	0.63	0.56	1.30
2D QWS	78.3	6117.5	0.41	0.43	2.38
3D QWS	46.7	901.5	0.43	0.34	2.41

TABLE V: Quantitative evaluation of filtering performance in San Francisco dataset.

Method	ENL	PolENL	EPI-H	EPI-V	TCD
Refined Lee	20.6	434.7	0.19	0.27	1.67
Extended sigma	6.9	377.6	0.39	0.41	0.58
Pretest	89.8	2081.8	0.20	0.28	1.46
2D QWS	231.2	3740.8	0.20	0.24	2.68
3D QWS	181.7	1159.5	0.17	0.28	2.56

computed by using training areas that are marked by horizontal lines in Fig. 3 ($\star$-2), while the EPI is computed by using training areas that are marked by vertical lines. The detection of point targets in the TCD calculation is performed in the same way as in [3]. All the metrics are calculated by averaging the metrics of four incident polarization states.

We can find that the 2D and 3D QWS show significantly higher ENL values than the conventional methods. In addition, the PolENL values of the 2D QWS are also much higher than those of the conventional methods. The proposed methods have higher speckle-reduction abilities because they filter all pixels in an entire image simultaneously in the wavelet domain, while the conventional methods use size-limited windows. The EPI values of the proposed methods are close to those of the refined Lee and pretest filters in the San Francisco dataset. However, the proposed methods show higher TCD values than the conventional methods.

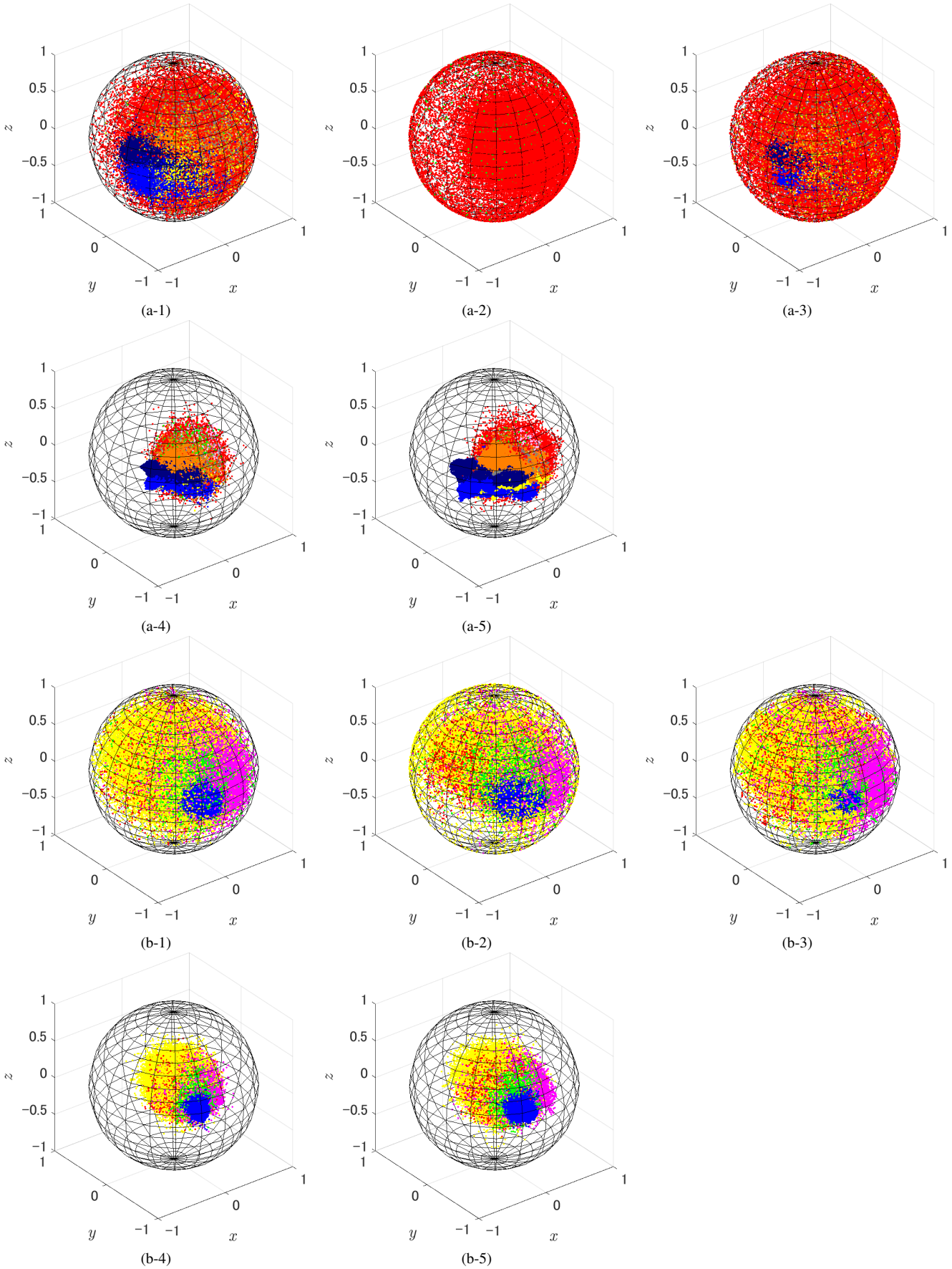

Fig. 6: Poincare-sphere plots of (a-⋆) Baltrum and (b-⋆) San Francisco datasets ((⋆-1) Refined Lee filter, (⋆-2) Extended sigma filter, (⋆-3) Pretest filter, (⋆-4) 2D QWS, and (⋆-5) 3D QWS).

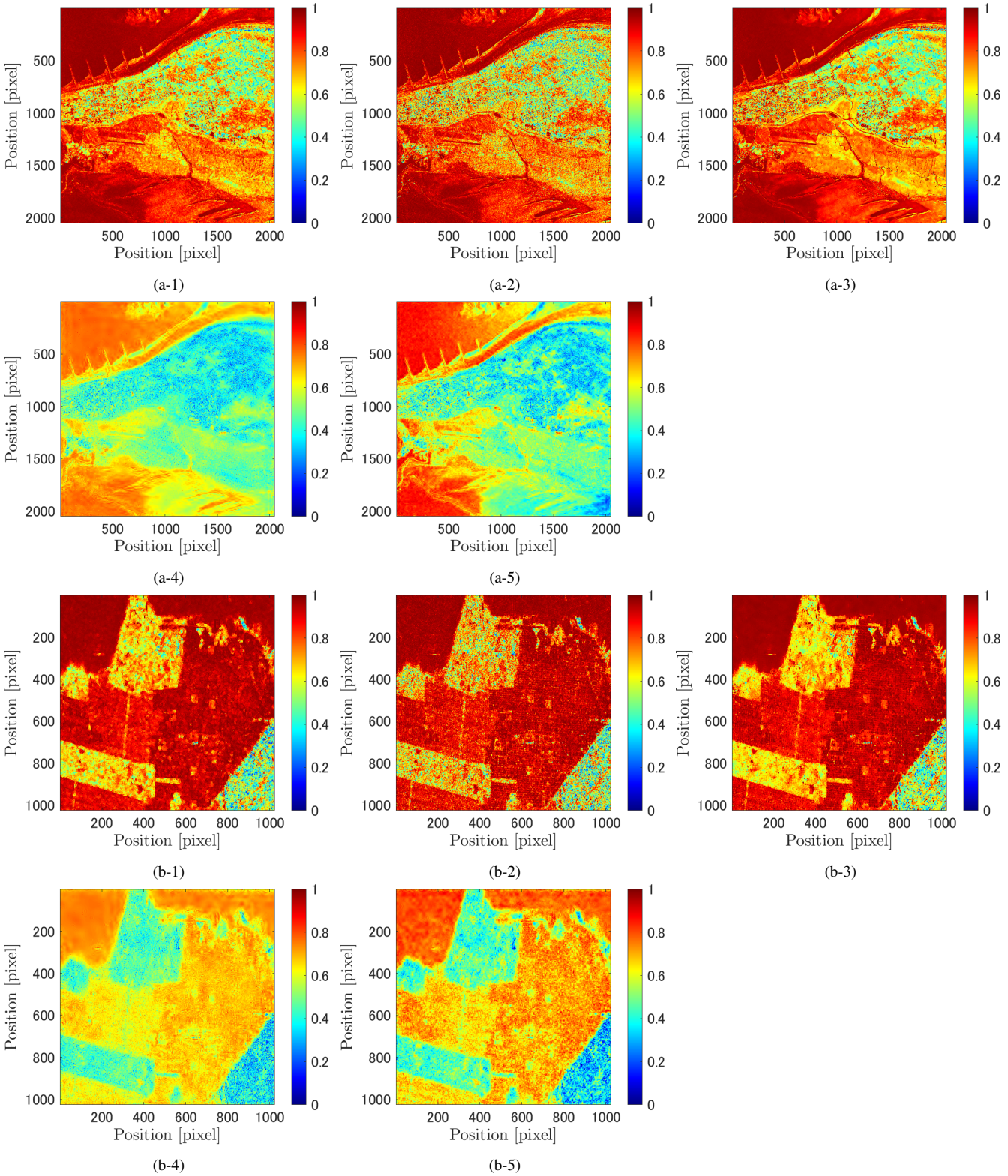

Fig. 7: DoP maps of (a-⋆) Baltrum and (b-⋆) San Francisco datasets ((⋆-1) Refined Lee filter, (⋆-2) Extended sigma filter, (⋆-3) Pretest filter, (⋆-4) 2D QWS, and (⋆-5) 3D QWS).

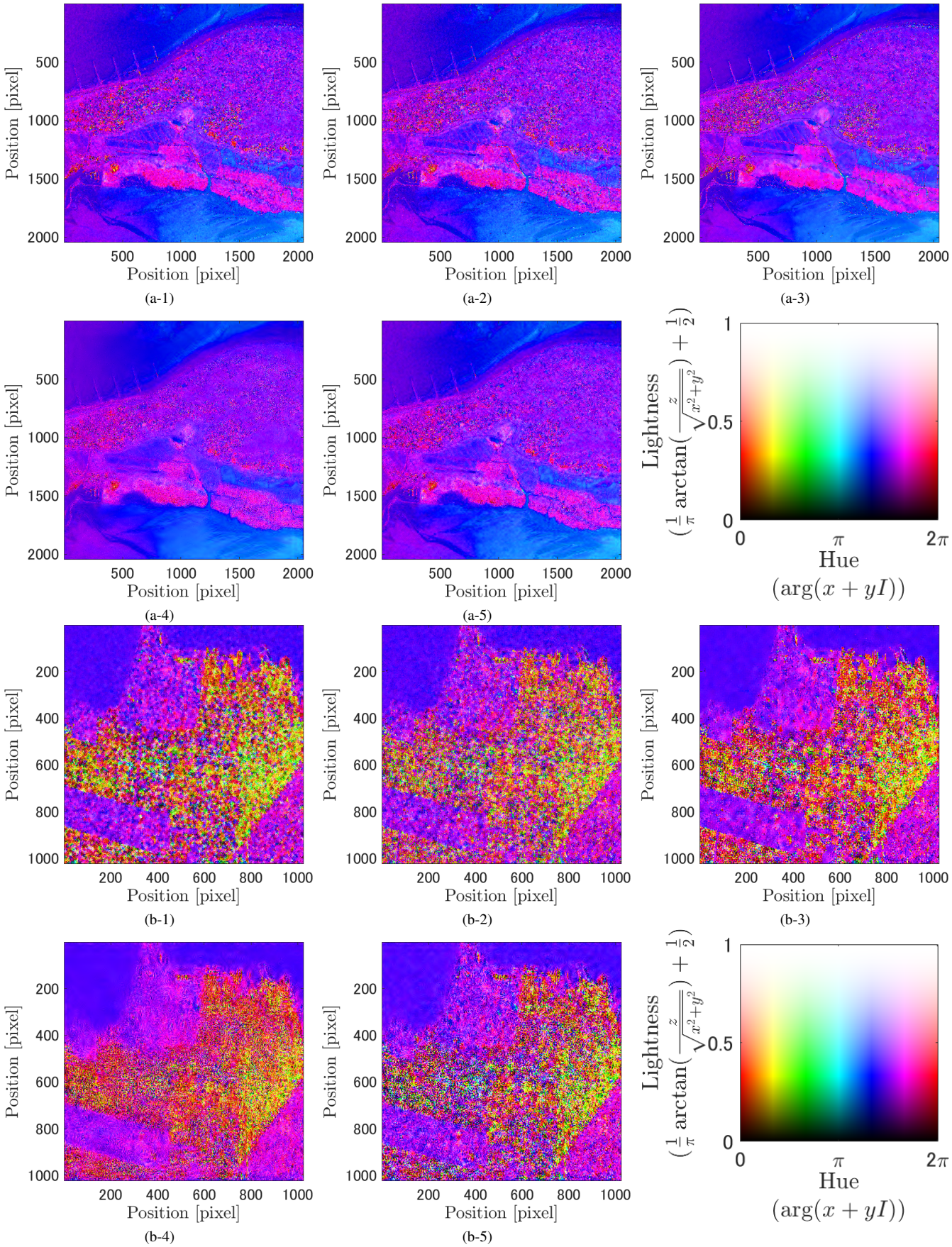

Fig. 8: Polarization-state maps of (a-⋆) Baltrum and (b-⋆) San Francisco datasets ((⋆-1) Refined Lee filter, (⋆-2) Extended sigma filter, (⋆-3) Pretest filter, (⋆-4) 2D QWS, and (⋆-5) 3D QWS).

TABLE VI: PolENL of each class in Baltrum dataset (TF: Tidal flat, W: Water, CS: Costal shrub, DV: Dense and high vegetation, WD: White dune, GD: Grey dune, CG: Couch grass, US: Upper salt marsh, LS: Lower salt marsh, S: Sand, and SE: Settlement).

Method	PolENL										
	TF	W	CS	DV	WD	GD	CG	US	LS	S	SE
Refined Lee	134.2	129.3	26.4	33.3	19.4	23.4	34.8	32.0	47.5	53.4	7.7
Extended sigma	104.9	103.6	19.8	19.2	18.2	22.3	23.5	30.7	28.9	55.1	7.8
Pretest	217.3	163.4	28.1	41.9	14.9	26.2	53.1	37.6	70.6	54.5	5.2
2D QWS	236.1	172.9	33.4	25.3	95.7	74.9	50.8	72.3	45.3	120.0	23.2
3D QWS	148.6	111.3	55.0	46.5	67.7	64.2	54.9	57.5	63.0	91.5	25.9

TABLE VII: PolENL of each class in San Francisco dataset (W: Water, V: Vegetation, HU: High-density urban, LU: Low-density urban, and D: Developed).

Method	PolENL				
	W	V	HU	LU	D
Refined Lee	303.3	24.4	26.2	33.9	7.8
Extended sigma	269.9	18.0	23.3	31.0	7.8
Pretest	1053.2	39.1	28.8	39.6	8.2
2D QWS	328.4	54.2	57.7	79.3	25.3
3D QWS	239.5	54.5	58.2	59.5	23.6

D. Analysis of filtered log Stokes vectors

1) Poincare-sphere plots: Fig. 6 shows the Poincare-sphere plots of the Baltrum and San Francisco datasets. Poincare vectors are calculated as

$$\begin{bmatrix} x \\ y \\ z \end{bmatrix} = \begin{bmatrix} \frac{\hat{g}_1^{\log}}{\hat{g}_0^{\log}} & \frac{\hat{g}_2^{\log}}{\hat{g}_0^{\log}} & \frac{\hat{g}_3^{\log}}{\hat{g}_0^{\log}} \end{bmatrix}^{\mathrm{T}} \tag{26}$$

In the plots of the 2D and 3D QWS, Poincare-vector lengths, that is, DoP values, are normalized to lie within [0,1]. The incident polarization state is the 135° linear polarized wave for both datasets. In the Poincare spheres of the conventional methods, there is high variance of polarimetric information. On the other hand, there is much less variance in the Poincare spheres of the 2D and 3D QWS.

Table VI and VII show the PolENL of each class in the Baltrum and San Francisco datasets, respectively. The PolENL is averaged over four incident polarization states. The 2D and 3D QWS show higher PolENL values for the White dune and Settlement classes in the Baltrum dataset. The Settlement class, as well as the White dune class, is a complex land cover type composed of different scattering mechanisms [26]. The proposed methods reduce the pixel-wise variance of polarimetric information due to complex land cover types. This property makes them suitable for the preprocessing of pixel-wise land cover classification. The 3D QWS present higher PolENL values than the 2D QWS for some vegetated classes, such as the Coastal shrub, Dense and high vegetation, and Couch grass classes. This suggests that the 3D QWS can extract the polarimetric features of vegetated areas more effectively than the 2D QWS.

2) DoP maps: Fig. 7 shows the DoP maps of the Baltrum and San Francisco datasets. The incident polarization state is the horizontal wave for both datasets. Again, the DoP values of the 2D and 3D QWS are normalized to lie within [0,1]. It can be found in the Settlement areas of the Baltrum dataset that the DoP values fluctuate in the DoP maps of the conventional methods. The DoP values of the 2D and 3D QWS are more constant in these areas. This indicates that the DoP values of the QWS represent features characterizing each land cover type, while those of the conventional methods represent more local features.

3) Polarization-state maps: Fig. 8 shows the polarization-state maps of the Baltrum and San Francisco datasets. The polarization states are represented by the hue-saturation-lightness (HSL) color space as

$$\begin{aligned} \mathrm{Hue} &= \arg(x + yI) \\ \mathrm{Saturation} &= 1 \\ \mathrm{Lightness} &= \frac{1}{\pi}\arctan\left(\frac{z}{\sqrt{x^2+y^2}}\right) + \frac{1}{2} \end{aligned} \tag{27}$$

where I is the imaginary unit of complex numbers. The incident polarization state is the 135° linear polarized wave for both datasets. It can be seen in Fig. 8(a-1), (a-2), and (a-3) that the polarization states in the Settlement areas fluctuate due to the existence of different scattering mechanisms. The polarization-state maps of the 2D and 3D QWS show less fluctuation in these areas. This means that the polarization states of the proposed methods, as well as the DoP values, are more effective for classifying complex land cover types than those of the conventional methods.

V. Conclusion

In this paper, we proposed context-aware PolSAR filters based on the 2D and 3D QWS. The proposed methods simultaneously suppress speckle noise and embed spatial-context information into filtered data. The experimental results showed that they achieve high classification accuracy by reducing the pixel-wise variance of polarimetric information due to complex land cover types. Since a large amount of labeled data is mostly unavailable for PolSAR land cover classification, the effective speckle suppression and feature extraction by the proposed methods will be increasingly important in the near future.

References

[1] Y. Otsuka, T. Shimada, R. Natsuaki, and A. Hirose, "Consideration on singular-point generating mechanisms by analyzing the effect of phase-and-polarization optimization in PolInSAR," *IEEE Journal of Selected Topics in Applied Earth Observations and Remote Sensing*, vol. 13, pp. 1625–1638, 2020.

[2] Y. Otsuka, R. Natsuaki, and A. Hirose, "Biquaternion Fourier domain filter for InSAR noise suppression by enhancing polarimetric-interferometric fringe patterns," *IEEE Transactions on Geoscience and Remote Sensing*, 2024.
[3] J.-S. Lee, T. L. Ainsworth, Y. Wang, and K.-S. Chen, "Polarimetric SAR speckle filtering and the extended sigma filter," *IEEE Transactions on Geoscience and Remote Sensing*, vol. 53, no. 3, pp. 1150–1160, 2014.
[4] G. Vasile, E. Trouvé, M. Ciuc, P. Bolon, and V. Buzuloiu, "Intensity-driven-adaptive-neighborhood technique for POLSAR parameters estimation," in *IEEE International Geoscience and Remote Sensing Symposium*, vol. 8, 2005, pp. 5509–5512.
[5] J. Chen, Y. Chen, W. An, Y. Cui, and J. Yang, "Nonlocal filtering for polarimetric SAR data: A pretest approach," *IEEE Transactions on Geoscience and Remote Sensing*, vol. 49, no. 5, pp. 1744–1754, 2010.
[6] C.-A. Deledalle, L. Denis, F. Tupin, A. Reigber, and M. Jäger, "NL-SAR: A unified nonlocal framework for resolution-preserving (Pol)(In) SAR denoising," *IEEE Transactions on Geoscience and Remote Sensing*, vol. 53, no. 4, pp. 2021–2038, 2014.
[7] D. Tucker and L. C. Potter, "Polarimetric SAR despeckling with convolutional neural networks," *IEEE Transactions on Geoscience and Remote Sensing*, vol. 60, pp. 1–12, 2022.
[8] A. G. Mullissa, C. Persello, and J. Reiche, "Despeckling polarimetric SAR data using a multistream complex-valued fully convolutional network," *IEEE Geoscience and Remote Sensing Letters*, vol. 19, pp. 1–5, 2021.
[9] H. Lin, K. Jin, J. Yin, J. Yang, T. Zhang, F. Xu, and Y.-Q. Jin, "Residual in residual scaling networks for polarimetric SAR image despeckling," *IEEE Transactions on Geoscience and Remote Sensing*, vol. 61, pp. 1–17, 2023.
[10] C. He, S. Li, Z. Liao, and M. Liao, "Texture classification of PolSAR data based on sparse coding of wavelet polarization textons," *IEEE Transactions on Geoscience and Remote Sensing*, vol. 51, no. 8, pp. 4576–4590, 2013.
[11] H. Bi, L. Xu, X. Cao, Y. Xue, and Z. Xu, "Polarimetric SAR image semantic segmentation with 3D discrete wavelet transform and markov random field," *IEEE Transactions on Image Processing*, vol. 29, pp. 6601–6614, 2020.
[12] A. Masjedi, M. J. V. Zoej, and Y. Maghsoudi, "Classification of polarimetric SAR images based on modeling contextual information and using texture features," *IEEE Transactions on Geoscience and Remote Sensing*, vol. 54, no. 2, pp. 932–943, 2015.
[13] J. Feng, Z. Cao, and Y. Pi, "Polarimetric contextual classification of PolSAR images using sparse representation and superpixels," *Remote Sensing*, vol. 6, no. 8, pp. 7158–7181, 2014.
[14] Y. Zhou, H. Wang, F. Xu, and Y.-Q. Jin, "Polarimetric SAR image classification using deep convolutional neural networks," *IEEE Geoscience and Remote Sensing Letters*, vol. 13, no. 12, pp. 1935–1939, 2016.
[15] A. Jamali, M. Mahdianpari, F. Mohammadimanesh, A. Bhattacharya, and S. Homayouni, "PolSAR image classification based on deep convolutional neural networks using wavelet transformation," *IEEE Geoscience and Remote Sensing Letters*, vol. 19, pp. 1–5, 2022.
[16] F. Shang and A. Hirose, "Quaternion neural-network-based PolSAR land classification in Poincare-sphere-parameter space," *IEEE Transactions on Geoscience and Remote Sensing*, vol. 52, no. 9, pp. 5693–5703, 2013.
[17] A. Hirose, F. Shang, Y. Otsuka, R. Natsuaki, Y. Matsumoto, N. Usami, Y. Song, and H. Chen, "Quaternion neural networks: A physics-incorporated intelligence framework," *IEEE Signal Processing Magazine*, vol. 41, no. 3, pp. 88–100, 2024.
[18] P. Fletcher and S. J. Sangwine, "The development of the quaternion wavelet transform," *Signal Processing*, vol. 136, pp. 2–15, 2017.
[19] P. Ginzberg and A. T. Walden, "Matrix-valued and quaternion wavelets," *IEEE Transactions on Signal Processing*, vol. 61, no. 6, pp. 1357–1367, 2012.
[20] Y. Otsuka, R. Natsuaki, and A. Hirose, "Proposal of a context-aware PolSAR filter based on quaternion wavelet shrinkage for efficient land cover classification," in *IGARSS 2025-2025 IEEE International Geoscience and Remote Sensing Symposium*, 2025, pp. 579–583.
[21] N. D. Dizon and J. A. Hogan, "Holistic processing of color images using novel quaternion-valued wavelets on the plane: A promising transformative tool," *IEEE Signal Processing Magazine*, vol. 41, no. 2, pp. 51–63, 2024.
[22] S. G. Mallat, "A theory for multiresolution signal decomposition: the wavelet representation," *IEEE Transactions on Pattern Analysis and Machine Intelligence*, vol. 11, no. 7, pp. 674–693, 1989.
[23] D. L. Donoho, "De-noising by soft-thresholding," *IEEE Transactions on Information Theory*, vol. 41, no. 3, pp. 613–627, 1995.
[24] N. Le Bihan and S. J. Sangwine, "Quaternion Toolbox for Matlab." [Online]. Available: http://qtfm.sourceforge.net/
[25] J.-S. Lee, M. R. Grunes, and G. De Grandi, "Polarimetric SAR speckle filtering and its implication for classification," *IEEE Transactions on Geoscience and Remote Sensing*, vol. 37, no. 5, pp. 2363–2373, 1999.
[26] S. Hochstuhl, N. Pfeffer, A. Thiele, S. Hinz, J. Amao-Oliva, R. Scheiber, A. Reigber, and H. Dirks, "Pol-InSAR-Island-A benchmark dataset for multi-frequency Pol-InSAR data land cover classification," *ISPRS Open Journal of Photogrammetry and Remote Sensing*, vol. 10, p. 100047, 2023.
[27] X. Liu, L. Jiao, F. Liu, D. Zhang, and X. Tang, "PolSF: PolSAR image datasets on San Francisco," in *International Conference on Intelligence Science*. Springer, 2022, pp. 214–219.
[28] F. Argenti, A. Lapini, T. Bianchi, and L. Alparone, "A tutorial on speckle reduction in synthetic aperture radar images," *IEEE Geoscience and Remote Sensing Magazine*, vol. 1, no. 3, pp. 6–35, 2013.
[29] J.-S. Lee, L. Jurkevich, P. Dewaele, P. Wambacq, and A. Oosterlinck, "Speckle filtering of synthetic aperture radar images: A review," *Remote Sensing Reviews*, vol. 8, no. 4, pp. 313–340, 1994.